



(LaSr)_xMnO₃ cathode stoichiometry effects on electrochemical performance in contact with AISI 441 steel interconnect

Kathy Lu*, Fengyu Shen, Rose Roberts, Grayson Doucette, Matthew McGuire, Wenle Li

Department of Materials Science and Engineering, Virginia Tech, Blacksburg, VA 24061, USA



HIGHLIGHTS

- Stoichiometry effect of LSMs on cathode/electrolyte interaction is studied.
- Polarization resistance is dominant for decreasing half-cell performance.
- A-site excessive LSM experiences stronger bonding with YSZ electrolyte.
- Cr first deposits and then is incorporated into the cathode by replacing Sr.
- A-site deficient LSM is preferred for cell performance improvement.

ARTICLE INFO

Article history:

Received 9 December 2013

Received in revised form

23 April 2014

Accepted 9 June 2014

Available online 17 June 2014

Keywords:

Solid oxide fuel cell

LSM cathode

Cathode degradation

Chromium diffusion

Stoichiometry

Interfacial interaction mechanism

ABSTRACT

Cathode plays an important role in solid oxide fuel cell performance. This work studies the stoichiometry effect of (LaSr)_xMnO₃ (LSM) cathode on its electrochemical behaviors at 800 °C by investigating the interfacial reaction of an AISI 441 interconnect/LSM electrode/yttria-stabilized zirconia (YSZ) electrolyte half-cell structure. Ohmic resistance and polarization resistance of the cathodes are analyzed by deconvoluting the electrochemical impedance spectroscopy (EIS) data. The results show that the polarization resistance is dominant for decreasing the half-cell performance. Microstructure and phase analyses show that A-site excessive LSM sample experiences stronger bonding with the YSZ electrolyte. Energy dispersive X-ray spectroscopy analyses reveal that Cr species first deposits and then is incorporated into the cathode perovskite structure by replacing Sr in the structure. Based on the above observations, the interaction mechanisms for the AISI 441 interconnect/LSM electrode/YSZ electrolyte tri-layer are proposed. Overall, the A-site deficient LSM stoichiometry is preferred for cell performance improvement.

© 2014 Elsevier B.V. All rights reserved.

1. Introduction

Solid oxide fuel cells (SOFCs) hold the greatest promise as a clean power generation device because of a combination of high efficiency, high energy and power densities, and fuel flexibility. Applications include on-board auxiliary power units, mobile power generators, and stationary power generation [1–5]. Miniaturized SOFCs are desired for powering long duration devices and remote communication electronics [6,7]. However, several technical issues need to be addressed in order to fully realize the promise of SOFCs. The most serious problems are the evaporative Cr species from the

interconnect that diffuse to the cathode, and the accompanying interfacial reactions at the electrolyte–cathode interface [8,9].

The interactions between the Cr-containing vapor species and the cathode have been recognized and investigated. However, there are considerable disagreements on the mechanism of Cr-containing species deposition on the cathode and at the electrode-air-electrolyte triple-phase boundaries (TPBs). Taniguchi et al. and Badwal et al. suggested that the deposition of Cr species is closely related to the oxygen activity at the TPBs; the deposition of Cr species is mainly caused by the electrochemical reduction of gaseous Cr-containing species to the solid Cr₂O₃ phase in competition with the O₂ reduction reaction on the cathode near the TPBs [10,11]. In contrast, Konyshova et al. believed that the interfacial degradation by Cr poisoning could be caused by (i) blocking of electrochemically active sites by electrochemical reduction of Cr-containing species at the TPBs, and (ii) decomposition of the

* Corresponding author. 211B Holden Hall, Materials Science and Engineering Department, Virginia Tech, Blacksburg, VA 24061, USA. Tel.: +1 540 231 3225; fax: +1 540 231 8919.

E-mail address: klu@vt.edu (K. Lu).

cathode by the formation of Cr-containing mixed oxide, driven by the thermodynamics without any influence of the electrical potentials [12]. Jiang et al. claimed that the deposition of Cr species depends strongly on the nature of the cathode materials and is most likely controlled by a non-electrochemical process [13,14]. The basis for Jiang's claim is that there is no intrinsic relationship between Cr species deposition and oxygen activity at the TPBs near the YSZ electrolyte; Cr deposition is basically controlled by chemical dissociation initiated by the nucleation reaction between the gaseous Cr species and the manganese species, in particular Mn^{2+} , in the cathode.

In addition, the role of the electrical current on the chemical reactions is still being debated [15,16]. It is unclear whether the Cr-containing species hinder electrochemical reactions at the TPBs or simply block the active sites on the cathode. If the main process is at the TPBs, then the electrical current effect needs to be thoroughly understood. If the deposition process is dominant, then the cathode stoichiometry and active surface site availability need to be studied, as these can substantially affect the interfacial compatibility and play important roles in SOFC performance and durability [17–19]. Currently there is a lack of material testing and characterization efforts to systematically answer these questions, especially when the LSM cathode stoichiometry varies.

In our previous work without an electric current, it has been shown that Cr species diffuses into the porous LSM layer and deposits on the LSM surface. The deposition occurs simultaneously with the LSM grain growth [20]. With an electric current, different LSM stoichiometry leads to different interfacial reactions and Cr deposition amounts. Mn is a critical species for the Cr deposition under polarization. Excessive Mn in LSM lessens the formation of La-containing phase at the YSZ/LSM interface and accelerates the Cr deposition. Deficient Mn amount in LSM leads to extensive interfacial reaction with YSZ, forming more La-containing phase and inhibiting Cr deposition [21]. For the Mn-excessive LSM sample, Sr-containing compound leads to a high Cr content at the YSZ/LSM interface. For the Mn-deficient LSM sample, on the other hand, the enrichment of La at the YSZ/LSM interface hinders the Cr deposition, leading to a very low Cr content [22].

In this study, LSM-based cathodes with different stoichiometry are fabricated. Synthesized $(La_{0.8}Sr_{0.2})_{1.0}MnO_3$ (noted as LSM 100), $(La_{0.8}Sr_{0.2})_{0.95}MnO_3$ (A-site deficient, noted as LSM 95), and $(La_{0.8}Sr_{0.2})_{1.05}MnO_3$ (A-site excessive, noted as LSM 105) are used as the cathodes to study the Cr species–electrode interaction at the TPBs. The electrochemical performance of the cathodes as well as the microstructures and composition changes at the LSM/YSZ interface are examined. Based on these efforts, the cathode degradation mechanism is proposed.

2. Experimental procedures

2.1. Synthesis of LSM powders

In this work, perovskite LSM powders were synthesized by a solid state reaction process [23]. $SrCO_3$ (99.9%, Sigma Aldrich, St. Louis, MO), La_2O_3 (99.98%, Alfa Aesar, Ward Hill, MA), and $MnCO_3$ (99.9%, Alfa Aesar, Ward Hill, MA) at designed composition ratios were mixed. The mixed powders (three compositions were made based on the stoichiometric ratio: LSM 95, LSM 100, and LSM 105) were ball-milled overnight and then sintered at 1400 °C for 15 h with a heating and cooling rate of 5 °C min⁻¹. The resulting powders were ball-milled overnight again to reduce the particle size, and a second sintering process at 1400 °C for 5 h was carried out with the same heating and cooling rate. The prepared powders were then ball-milled for 3 days to further reduce the particle size and improve the performance of the resulting cathodes.

2.2. Assembly of AISI 441/LSM/YSZ tri-layer

The LSM powders (56.8 wt%) were mixed and ball-milled with microcrystalline cellulose (pore forming agent, 5.7 wt%, Spectrum, Gardena, CA), ethyl cellulose (binder, 1.1 wt%, Acros Organics, New Jersey), and α -terpineol (solvent, 36.4 wt%, Sigma–Aldrich, St. Louis, MO) for 1 h to make pastes for screen printing. The prepared pastes were screen printed on 8 mol% YSZ (Nextech Materials, Lewis Center, OH) substrates, using a #330 mesh. The screen printed pastes were square-like with ~0.5 cm² area. The LSM/YSZ couples were kept at 200 °C for 3 h and at 400 °C for 1 h to burn out the binder, pore-forming agent, and solvent. Afterwards, these bi-layers were sintered at 1150 °C for 2 h, with a heating and cooling rate of 1 °C min⁻¹. The thickness of the LSM electrodes after sintering was ~30 μ m, measured through scanning electron microscopy (SEM) images.

AISI 441 ferritic stainless steel pieces (ATI Allegheny Ludlum Corporation, Brackenridge, PA) were used as the interconnect material and were cut into rectangular substrates (area: 10 × 10 mm², thickness: 2.08 mm). In order to remove the oxidized layer (if any) and obtain a scratch free flat surface, the steel pieces were polished to optical finish, and ultrasonically cleaned with water and ethanol. The polished AISI 441 alloy piece was placed on the LSM electrode side of the LSM/YSZ bi-layer and the configuration of the tri-layer was shown in our previous paper [20].

2.3. Thermal treatment under current load

In order to investigate the electrochemical behavior of the LSM cathodes, AISI 441/LSM/YSZ tri-layers were heated to 800 °C, using a tube furnace (1730-20 HT Furnace, CM Furnace Inc. Bloomfield, NJ) in dry air environment. Afterwards, the tri-layers were cathodically polarized under a constant current density of 200 mA cm⁻², using a potentiostat (VersaSTAT 3, Princeton Applied Research, Oak Ridge, TN). A platinum mesh was placed in-between the LSM porous layer and the AISI 441 interconnect to optimize the current distribution, and the electrodes were connected by Pt wires along with Pd paste. The electrochemical impedance spectroscopy (EIS) testing program used was a multi-loop process. In each loop, the EIS test was carried out from 100 kHz to 0.025 Hz. The amplitude was 10 mV. After that, a current density of 200 mA cm⁻² was applied to mimic the working condition of the fuel cell. EIS data were recorded every 5 h during the thermal treatment. Detailed experimental setup has been provided before and can be found elsewhere [21,24].

2.4. Characterization and performance testing

The microstructures of the cathode and the LSM/YSZ interfaces were examined by a field emission SEM (LEO1550, Carl Zeiss MicroImaging Inc., Thornwood, NY), with a 3 nm Au–Pt layer coating applied before imaging. The phase development at the LSM/YSZ interfaces was carried out by X-ray diffraction (XRD, X'Pert PRO diffractometer, PANalytical B.V., EA Almelo, The Netherlands). The energy dispersive X-ray spectroscopy module (EDS, Bruker AXS, MiKroanalysisGmbH, Berlin, Germany) attached to the SEM was used to analyze elemental distributions throughout the cathodes after the EIS test.

3. Discussion

3.1. Electrochemical behaviors

Impedance spectra of all three LSM cathodes after 5 h, 50 h, and 100 h of thermal treatment are plotted in Fig. 1(a)–(c), respectively.

The data in-between the above time points show a consistent trend and are omitted for clarity. As shown, the curve for the 5 h thermal treatment samples has a more semi-circle shape, while the curves for the 50 h and 100 h thermal treatment samples display asymmetric shapes with more slanting on the left side. The slanted shapes of the curves persist for the rest of the thermal treatment duration. However, no shoulder is observed on the right side of the EIS curves. As for the impedance values, LSM95 has the smallest semi-circle during the entire thermal treatment process. Also, all the semi-circles shrink with time (i.e. the left intercepts on the horizontal axis are roughly fixed while the right ones become smaller with the thermal treatment time increase, the heights of the curves also decrease). During the EIS test, the decreasing rates of the semi-circles are different from each other. Overall, large impedance is observed for all the LSM samples, which have been recognized as the main factor of compromising cell performance when LSM is used as the cathode.

In order to correlate the EIS spectra with the mechanisms of the LSM cathode evolution, an equivalent circuit $R_\Omega(R_HCPE_H)(R_LCPE_L)$ (Fig. 2) has been used to fit the spectra and obtain deconvoluted arcs at different frequencies. The spectrum for the 50 h thermally

treated LSM 100 sample is deconvoluted and shown in Fig. 3 as an example. In the circuit, R_Ω is the ohmic resistance from the cathode, the Pt wires, and the Pd paste; R_H and R_L refer to the polarization resistances at high and low frequencies, respectively, while CPE_H and CPE_L are constant phase elements corresponding to each frequency range.

Fig. 4(a)–(c) shows the R_Ω , R_H , and R_L changes for the LSM 95, LSM 100, and LSM 105 samples after different hours of thermal treatment at 800 °C under 200 mA cm⁻² electric load. In general, there are no large changes for the ohmic resistance throughout the thermal treatment process. The R_Ω values are ~2.4–2.6 Ω cm², 5.9–10.5 Ω cm², and 3.8–6.5 Ω cm² respectively for the LSM 95, LSM 100, and LSM 105 samples. The largest ohmic resistance values and fluctuations happen for the LSM 100 sample. This means the ohmic resistance for the stoichiometric LSM formula is the most undesirable. However, the differences are not large compared to the polarization resistance and the relatively stable nature means the ohmic resistance is not the dominant factor influencing the cell performance.

For the high frequency polarization resistance R_H and low frequency polarization resistance R_L , the values are at least several times higher compared to the ohmic resistance for all the samples as shown in Fig. 4. These two resistance components have an overwhelming effect on the cell behaviors. To improve the LSM cathode performance, reducing polarization resistance (both high frequency and low frequency) is the key.

For all three LSM cathodes, there is a drastic decrease in the polarization resistance in the first 50 h of the thermal treatment. For LSM 95, R_H decreases from 29 Ω cm² to 20 Ω cm². For LSM 100, R_H decreases from 96 Ω cm² to 36 Ω cm². For LSM 105, R_H decreases from 64 Ω cm² to 24 Ω cm². After 50 h of thermal treatment, R_H decreases slowly. The values are 20–16 Ω cm², 36–23 Ω cm², and 24–22 Ω cm² for the LSM 95, LSM 100, and LSM 105 samples, respectively from 50 h to 100 h of thermal treatment. The R_L changes show the same trend as R_H with faster polarization resistance decrease in the initial stage of the thermal treatment. In the first 50 h of thermal treatment, R_L decreases from 66 Ω cm² to 22 Ω cm², 167 Ω cm² to 39 Ω cm², and 117 Ω cm² to 28 Ω cm² for the LSM 95, LSM 100, and LSM 105 samples, respectively. After 50 h of thermal treatment, R_L also decreases slowly. The values are 22–16 Ω cm², 39–25 Ω cm², and 28–22 Ω cm² for the LSM 95, LSM 100, and LSM 105 samples, respectively. Overall, under the same thermal treatment condition, the LSM 100 sample shows the highest polarization resistance (both R_H and R_L) while the LSM 95 sample shows the lowest. Since the ohmic resistance is also the highest for the LSM 100 cathode and lowest for the LSM 95 cathode, it can be concluded that LSM 95 (A-site deficit) is the most desirable LSM composition.

Interestingly, for all three LSM samples, the R_H and R_L reach about the same values at the end of the thermal treatment. An encouraging observation is that both high frequency polarization resistance R_H and low frequency polarization resistance R_L decrease with the thermal treatment and stabilize at longer thermal treatment time. This means the cell performance should improve or at least stay stable with use, which is much desired for the cell stack long term operation.

3.2. Microstructure and composition analysis

Even though the microstructures, phases, and compositions at the LSM/YSZ interface before the thermal treatment have been analyzed [21,22,25], as a baseline, the microstructures for all the three LSM cathodes are characterized. All the LSM samples have similar microstructures and only the image for the LSM 100 green sample is shown in Fig. 5(a) and the image for the LSM 100 sample

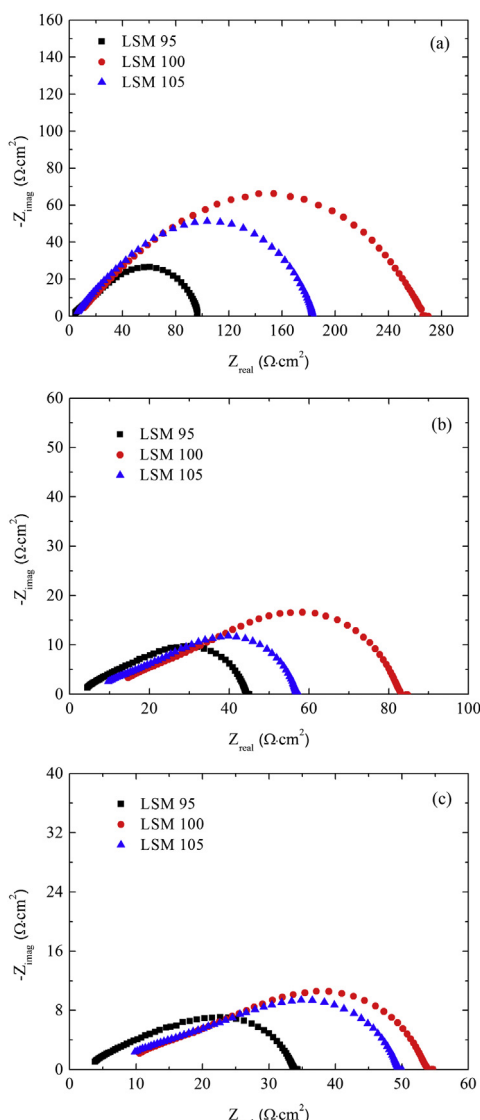


Fig. 1. Impedance spectra of LSM electrodes (LSM 95, LSM 100, and LSM 105) under 200 mA cm⁻² current load after thermal treatment for: (a) 5 h, (b) 50 h, and (c) 100 h.

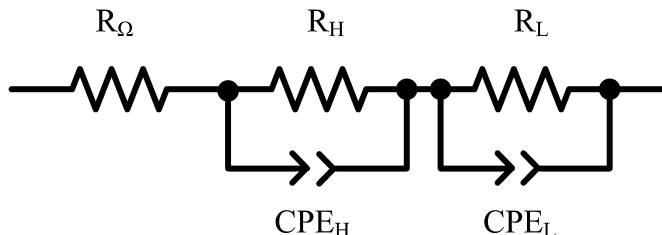


Fig. 2. The equivalent circuit used for fitting the EIS spectra in this study.

before the thermal treatment is shown in Fig. 5(b). In general, a large number of the LSM particles are elongated and the porous microstructure is homogeneous. Most of the grains are $\sim 2 \mu\text{m}$ size while some large ones are close to $10 \mu\text{m}$. Sintering of the LSM electrode onto the YSZ electrolyte before the thermal treatment causes slight microstructure coarsening.

The XRD patterns for clean YSZ electrolyte and different YSZ interfaces in contact with the LSM cathodes after the 100 h thermal treatment are shown in Fig. 6. For the LSM 95 sample, no new phase can be identified at the LSM/YSZ interface even though residuals from the LSM electrode can be easily seen in the SEM image (Fig. 7(a)). For the LSM 100 sample, some new diffraction peaks appear but are too weak to be indexed. For the LSM 105 sample, new peaks are observed and the new phase is indexed as $\text{La}_{0.7}\text{Sr}_{0.3}\text{MnO}_3$. Some of the new peaks coincide with those from the LSM 100 sample. This means that the interaction of the LSM 105 sample with the YSZ electrolyte is the same as that for the LSM 100 sample but the extent is stronger. When the LSM electrode is detached from the YSZ electrolyte after the thermal treatment, more LSM 105 residual has been kept on the YSZ side. It should also be pointed out that XRD is not a sensitive technique for low quantity phase detection. Even though no new phase is detected for the LSM 95 sample, it does not mean that there is no new species or interaction at the interface. The EDS analysis below shows more interactions at the interface.

Fig. 7 shows the SEM images of the interface between the LSM cathodes and the YSZ electrolyte after 100 h of thermal treatment. For the LSM 95 sample (Fig. 7(a)), the residuals are widespread on the YSZ surface. However, the sizes are relatively small. For the LSM 100 sample (Fig. 7(b)), the residuals are more concentrated with larger sizes; most of the YSZ surface is exposed. For the LSM 105

sample (Fig. 7(c)), both small and large size residuals are present and the coverage on the YSZ surface is higher than that of the LSM 100 sample. These interfacial particles indicate that the LSM electrodes with different stoichiometry have different extent of interaction with the YSZ electrolyte. The LSM 105 electrode interacts more extensively with the YSZ electrolyte than the LSM 100 electrode, consistent with the XRD results in Fig. 6. Based on the particle size and morphology, the YSZ interaction with the LSM 95 electrode follows a different mechanism with more widespread residual yet less defined phases.

The elemental distributions at the LSM95/YSZ interface are shown in Fig. 8 for the same region shown in Fig. 7(a). The distributions of the elements are depicted by colors. The blue (in web

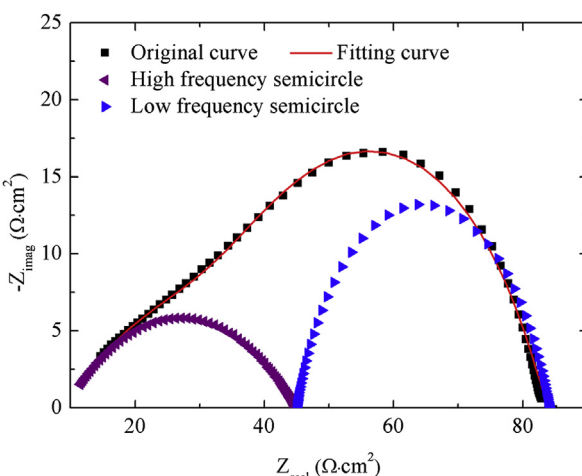


Fig. 3. An example deconvolution of the impedance spectrum for the 50 h thermally treated LSM 100 sample.

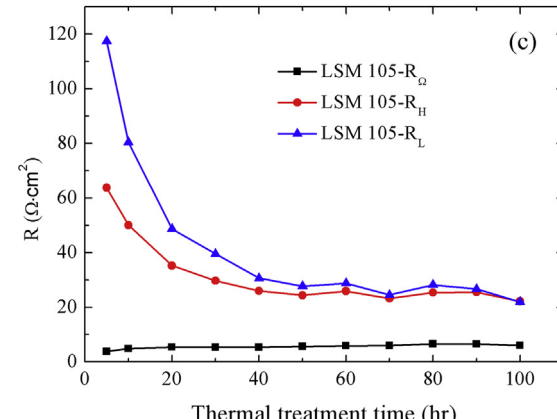
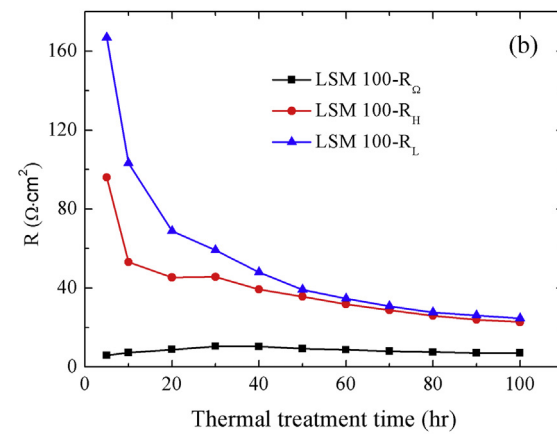
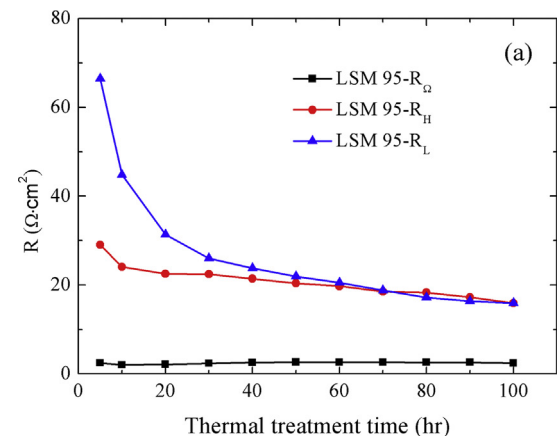


Fig. 4. Ohmic and polarization resistance changes for (a) LSM 95, (b) LSM 100, and (c) LSM 105 samples after different time of thermal treatment.

version) color represents La (Fig. 8(a)); the purple (in web version) color represents Mn (Fig. 8(b)); the red (in web version) color represents Sr (Fig. 8(c)); and the gold (in web version) color represents Cr (Fig. 8(d)). Elements La and Mn have the most consistent distributions. Sr element has opposite distribution as the above two elements, which means lower Sr concentration in the enriched regions for La and Mn elements. Cr distribution follows the same trend as that of La and Mn. However, the distribution is generally more diffused, consistent with the SEM morphology shown in Fig. 7(a). This analysis indicates that Cr diffuses from the AISI 441 interconnect, crosses the LSM cathode, and deposits at the LSM/YSZ triple phase boundaries. The interaction of Cr with LSM at the TPBs (as to be discussed later) leads to the depletion of Sr in the LSM structure.

The elemental distributions for the LSM 100/YSZ interface after 100 h of thermal treatment are shown in Fig. 9 for the same region shown in Fig. 7(b). The distribution consistency among La, Mn, and Cr is more obvious (Fig. 9(a), (b), and (d)). The Sr distribution is in general opposite those of La, Mn, and Sr (Fig. 9(c)). However, the low Sr concentration zones often expand beyond the La-, Mn-, and Cr-enriched regions. In our prior studies on LSCF, it has been observed that La and Fe distributions are largely complementary to those of Cr and Sr; the Sr- and Cr-rich regions are La- and Fe-deficient [24]. Apparently, LSM and LSCF cathode degrade in different mechanisms in the presence of Cr. For LSCF, Cr extracts Sr from the perovskite lattice structure and forms new species with it. In LSM, Cr replaces Sr in the LSM structure; Sr thus segregates out and stays most likely as SrO away from LSM. This degradation process is less likely when the LSM stoichiometry is A-site deficient (LSM 95), which also means when Sr is slightly deficient. Since La also resides at the A-sites, the Sr extraction from the perovskite structure indicates that Sr is less stable than La in the LSM lattice.

Fig. 10 shows the elemental distributions for the LSM 105/YSZ interface after 100 h of thermal treatment, for the same region shown in Fig. 7(c). In general, different elements have the same distribution trend as those of the LSM 95 and LSM 105 samples. However, a new feature is the peripheral distribution of Cr around La- and Mn-rich regions. This observation indicates that Cr deposits at the TPBs first before diffusing into the LSM lattice structure to replace Sr. The higher concentrations of the elemental species (brighter colors) are also consistent with the XRD data in Fig. 6. This means that A-site excessive LSM 105 induces more Cr deposition at TPBs and thus more cathode/electrolyte interfacial reaction and elemental segregation.

The analysis on elemental distributions at the LSM/YSZ interfaces confirms that Cr species diffuses during the thermal treatment and explains different features at the LSM/YSZ interfaces. However, the amounts of Cr-containing phases are too small to be detected by XRD after the thermal treatment. Despite the obvious elemental re-distributions based on the EDS analysis, it is not significant enough to form substantial amounts of new phases yet.

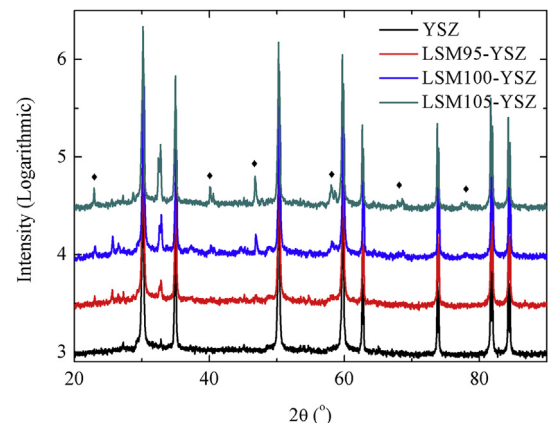


Fig. 6. XRD patterns for pure ZrO₂ and different ZrO₂ interfaces in contact with the LSM cathodes.

Although the EDS mapping results in Figs. 8–10 provide direct observation about elemental distribution, quantitative elemental distribution data need to be obtained through EDS area quantification. In Fig. 7, the analyzed areas for each sample are labeled as (a)–(e) based on the regions with the highest amount of LSM residuals, the intermediate amount, and the least amount. Each area is approximately $5 \times 5 \mu\text{m}^2$ in size. Taking O, Zr, Y, La, Sr, Mn, Cr into consideration, the concentration for each element can be quantified. For the LSM 95 sample, the highest Cr concentration (at location (a)) is 2 at%; the lowest Cr concentration (at location (d)) is 0.34 at%; the average Cr concentration is 1.21 at%. For the LSM 100 sample, the highest Cr concentration (at location (a)) is 0.07 at%; the lowest Cr concentration (at location (e)) is 0 at%; the average Cr concentration is 0.02 at%. For the LSM 105 sample, the highest Cr concentration (at location (a)) is 0.75 at%; the lowest Cr concentration (at location (d)) is 0.04 at%; and the average Cr concentration is 0.34 at%. The above results indicate that the LSM 95 sample is most susceptible to Cr deposition, the LSM 105 sample the second, and the LSM 100 sample the least. These findings are consistent with our earlier work for the LSM electrode [21]. Mn is a critical species for the Cr deposition to occur under polarization. Excessive Mn in LSM (for the LSM 95 sample) lessens the formation of La-containing phase at the YSZ/LSM interface (La content is 4.14 at% and the Mn content is 2.72 at%) and accelerates Cr deposition. At the same time, Cr distribution is more diffused. Deficient Mn in LSM (the LSM 105 sample) leads to stronger interfacial reaction with YSZ, forming more La-containing and Sr-containing phase (6.4 at% La and 1.87 at% Sr highest among the three LSM cathodes) and inhibiting Cr diffusion over the interface. As a result, Cr deposition is more confined at TPBs. The lowest Cr content sample (LSM 100) also has high amounts of Mn (6.4 at%) and La (7.94 at%). In addition,

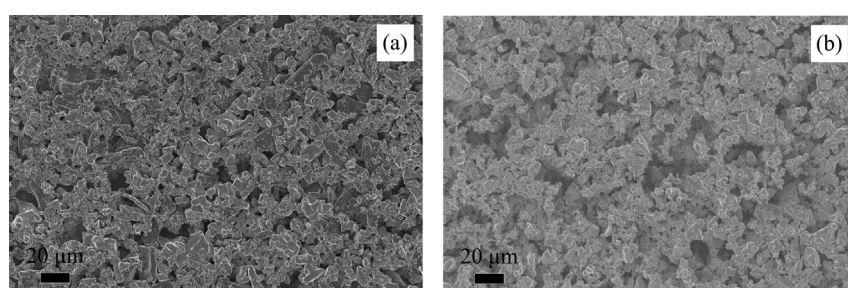


Fig. 5. Microstructures for the LSM 100 sample at green state (a) and before the thermal treatment (b).

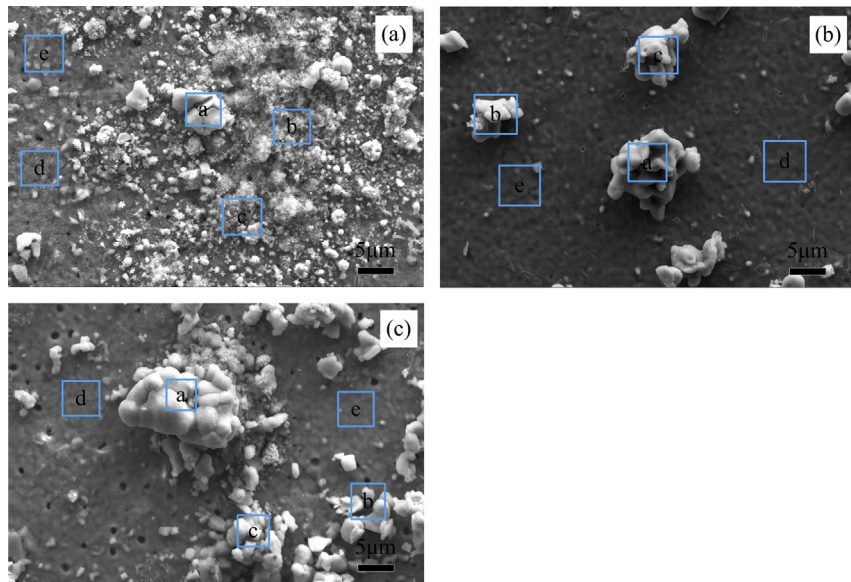


Fig. 7. Microstructures of the YSZ surfaces (i.e. the surfaces in contact with the LSM electrodes) after 100 h of thermal treatment: (a) LSM 95, (b) LSM 100, and (c) LSM 105.

Mn-deficient sample (LSM 95) has the least Sr segregation while the Mn-excessive sample (LSM 105) has the most Sr segregation.

From a different aspect, the higher Cr content at the LSM/YSZ interface does not directly lead to the poorest cathode electrochemical performance as shown in Fig. 11. The LSM 95 sample has the lowest total resistance throughout the thermal treatment process even though it has the highest concentration of Cr; the LSM 105 sample has intermediate resistance, and the LSM 100 sample has the highest resistance even though the Cr content is the lowest. This means that in addition to the Cr species diffusion to the cathode/electrolyte interface, the exact formats of the LSM electrodes and the Cr-containing species at the YSZ interface play a critical role in the cathode electrochemical performance.

3.3. Interaction mechanisms between AISI 441 and LSM cathodes

During the EIS test, the ohmic resistance of the cathode is governed by small polaron conduction (i.e. adiabatic-hopping of p-type polaron: X^{4+}) [26,27]. Theoretically, the concentration of small polarons increases with Sr^{2+} [16,17]. As this A-site species increases, some X^{3+} ions should be oxidized to form X^{4+} [27], which should improve the electrical conductivity of the electrode from LSM 95 to LSM 105. However, the LSM/YSZ interfacial effects seem to be play an important role compared to the bulk of the cathodes. As shown in Fig. 12, the average ohmic resistance actually increases from $2.4 \Omega \text{ cm}^2$ for the LSM 95 sample, to $8.2 \Omega \text{ cm}^2$ for the LSM 100 sample, and to $5.6 \Omega \text{ cm}^2$ for the LSM 105 sample. As discussed in

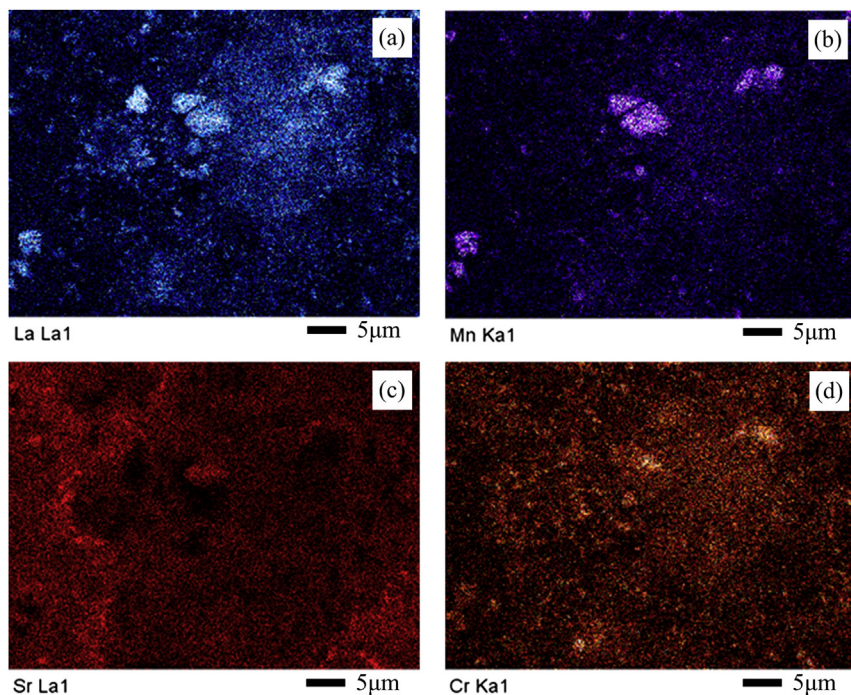


Fig. 8. EDS mapping showing elemental distributions of thermally treated LSM 95/YSZ interface: (a) La, (b) Mn, (c) Sr, (d) Cr.

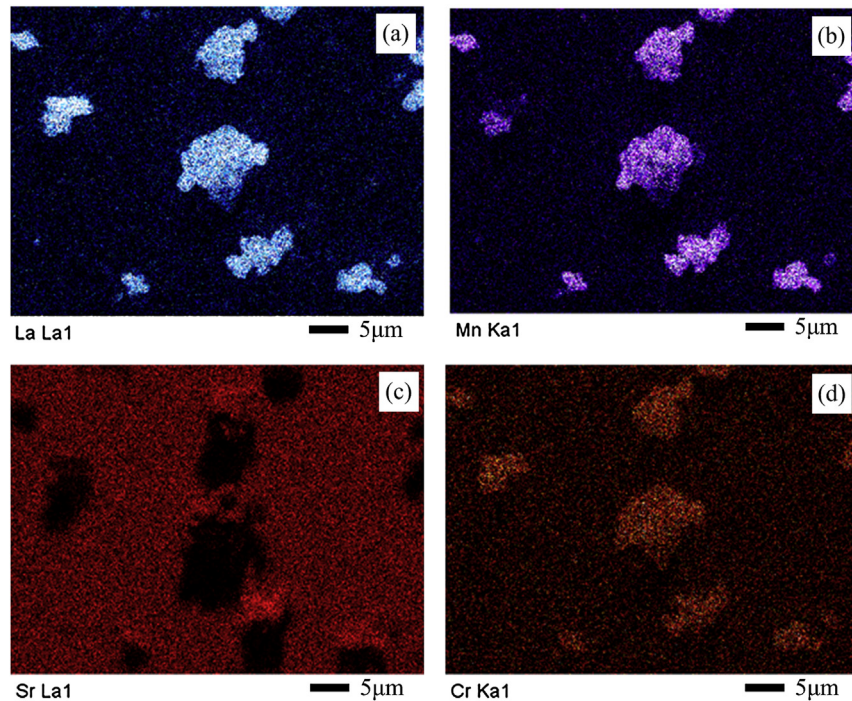


Fig. 9. EDS mapping showing elemental distributions of thermally treated LSM 100/YSZ interface: (a) La, (b) Mn, (c) Sr, (d) Cr.

Section 3.2 (Figs. 8–10), the areas rich in Cr are also rich in La and Mn but deficient in Sr. The less extraction of Sr^{2+} from the LSM 95 perovskite structure leads to less ohmic resistance increase at the interface. LSM 100 has an intermediate extent of elemental diffusion/re-distribution. More Sr extraction increases the ohmic resistance. Even though LSM 100 is the most Cr-diffusion resistant

composition among the three electrodes during the 100 h thermal treatment (lowest Cr content), the ohmic resistance does increase before it stabilizes with longer thermal treatment time. For the LSM 105 sample, Sr extraction may have been offset somehow by the excessive A-sites and the ohmic resistance stays intermediate. Regardless, during the thermal treatment, the ohmic resistance is

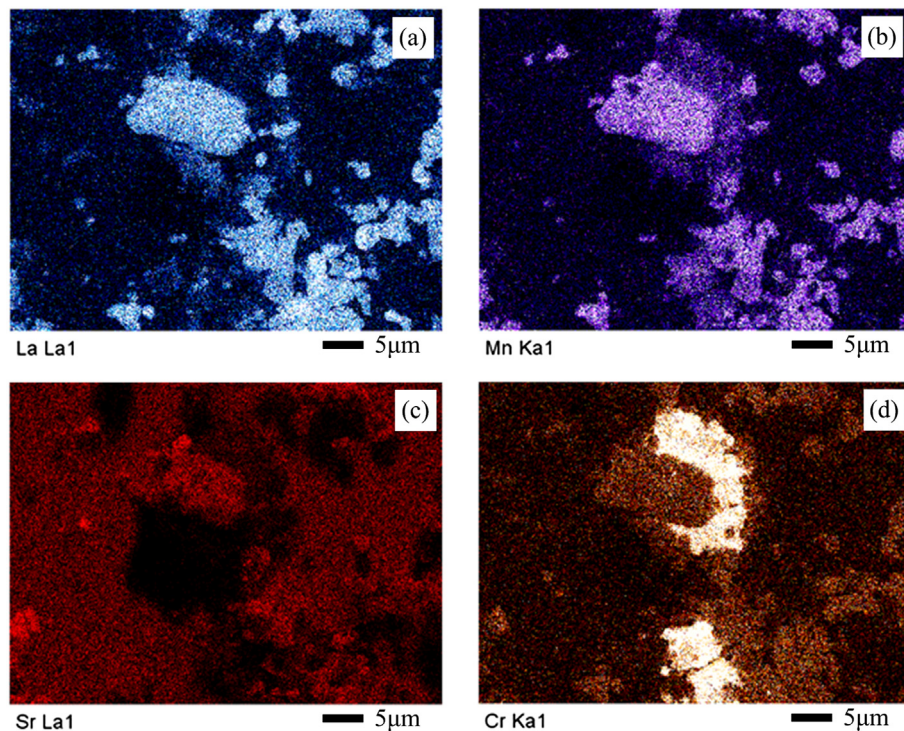


Fig. 10. EDS mapping showing elemental distributions of thermally treated LSM 105/YSZ interface: (a) La, (b) Mn, (c) Sr, (d) Cr.

relatively low for all the three cathodes. This means the conductivity from the polarons in the LSM bulk and LSM/YSZ interface is not significantly compromised and the ohmic resistance does not contribute significantly to the overall resistance of the cathodes.

The low frequency polarization resistance of the LSM cathode is related to oxygen adsorption on the cathode, dissociation at the cathode, and oxygen ion surface diffusion [28,29]. As seen in Fig. 13, both LSM 95 and LSM 105 off-stoichiometry samples have lower low frequency polarization resistance compared to the stoichiometric LSM 100 sample. The A-site deficient LSM 95 sample has the lowest low frequency polarization resistance. This can be understood as follows. As shown in Figs. 5–7, the Sr distribution is more dispersed in the A-site deficient electrode (LSM 95) than in the A-site exact and excessive electrodes (LSM 100 and LSM 105). The Cr distribution in LSM 95 also has some overlapping regions with that of element La. Since La species always sits at the A-site, this evidence suggests that Cr takes some A-sites in LSM 95 and participates in the LSM perovskite structure. The elemental segregation problem exerts the smallest influence on the LSM 95 electrical conductivity. With the thermal treatment time increase, the LSM grains become more connected. The surface diffusion of the O^{2-} ions becomes easier and thus the low frequency polarization resistance decreases. For LSM 100, the more severe leaching of Sr^{2+} from the perovskite structure adversely affects the oxygen incorporation into the cathode and the subsequent surface diffusion, which contributes to the low frequency polarization resistance increase. For LSM 105, the low frequency polarization resistance is intermediate; this is because Cr deposits on the cathode surface instead of extracting Sr out from the LSM lattice. The blocking effect is not as detrimental as the extraction of Sr species.

The high frequency polarization resistance corresponds to O^{2-} incorporation into the electrode and its transport in the cathode structure [28]. Fig. 14 shows the changes of high frequency polarization resistance for LSM 95, LSM 100, and LSM 105 samples. For A-site deficient electrode LSM 95, the A-site deficiency itself would generate more oxygen ions than the stoichiometric electrodes. The O^{2-} transport in the LSM lattice structure should be the highest. With the thermal treatment time increase, the LSM 95 network should be more connected and facilitate the O^{2-} transport, thus the high frequency polarization resistance decreases with the thermal treatment. For LSM 100, extraction of Sr^{2+} by Cr from the perovskite

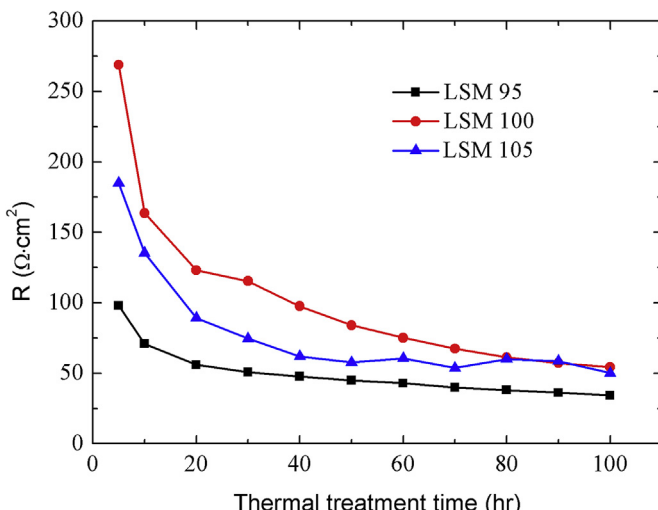


Fig. 11. Total resistance changes for the LSM 95, LSM 100, and LSM 105 samples after different time of thermal treatment.

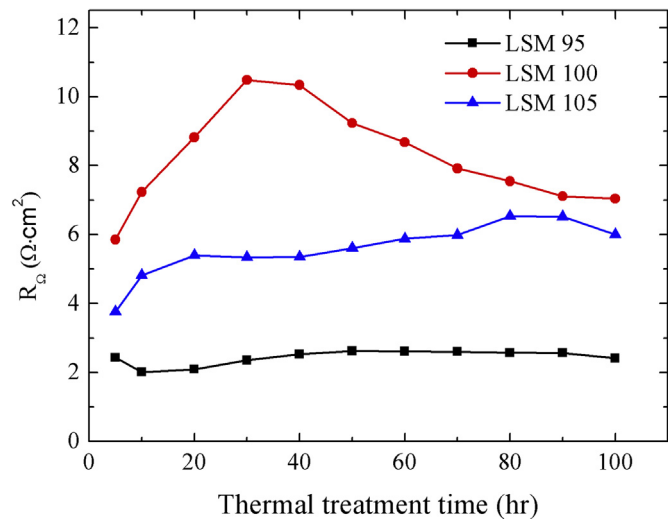


Fig. 12. Ohmic resistance changes for the LSM 95, LSM 100, and LSM 105 samples after different time of thermal treatment.

crystal structure adversely affects the oxygen incorporation into the cathode and the subsequent diffusion. As a result, the high frequency polarization resistance increases for LSM 100. However, the decreasing trend with the thermal treatment time is maintained. For LSM 105, Cr deposition on the LSM surface does not lead to as much impact on the LSM lattice structure as it has been for the LSM 100 sample. In addition, the presence of the excessive A-sites should be beneficial for O^{2-} transport; thus, the high frequency polarization resistance is intermediate. Again, the more connected LSM 105 network decreases the high frequency polarization resistance with the thermal treatment time.

In the literature, the interaction between the Mn^{2+} ions and the gaseous CrO_3 species has been claimed to cause the formation of $Cr-Mn-O$ nuclei, which in turn lead to the formation of Cr -containing spinel [28]:



If the Cr gas species is $CrO_2(OH)_2$ and the cathode is $(La,Sr)MnO_3$ (LSM), the chemical reaction at the interface has been claimed to be [30]:

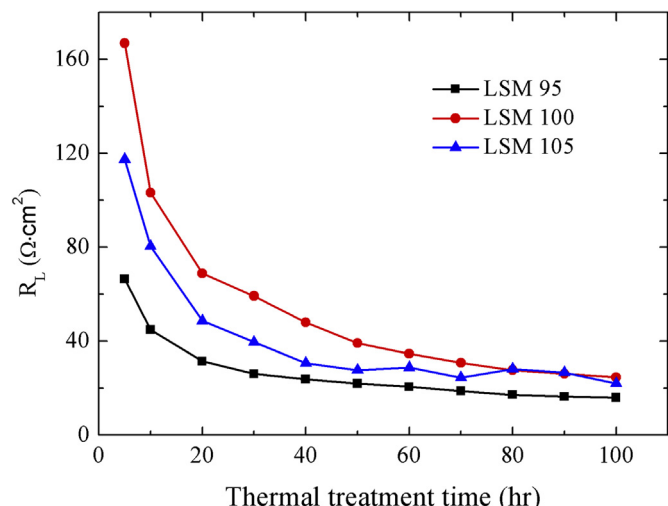


Fig. 13. Low frequency polarization resistance changes for LSM 95, LSM 100, and LSM 105 samples after different time of thermal treatment.

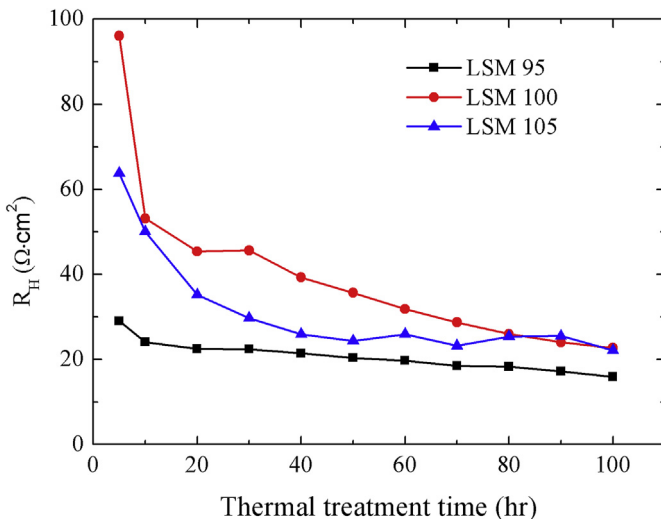
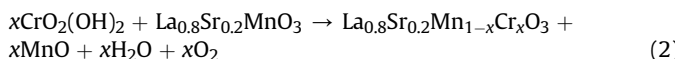
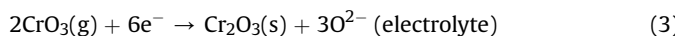


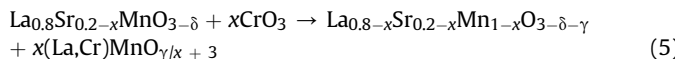
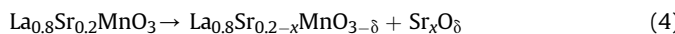
Fig. 14. High frequency polarization resistance changes for LSM 95, LSM 100, and LSM 105 samples after different time of thermal treatment.



However, our work indicates that the Cr species interaction with the cathode at the TPBs is different. Figs. 8–10 show two independent processes of Cr interaction at the LSM/YSZ interface: one is Cr deposition on the surface of LSM; another is interaction with LSM species on the LSM/YSZ interface (TPBs) by electrochemical process. When Cr reaches the surface of the LSM, we can consider it as the following process [31,32]:



Cr_2O_3 may simply deposit. Differently, the Cr species can replace the Sr species. The reaction is conjectured to be:



Equations (4) and (5) also explain why $\text{La}_{0.7}\text{Sr}_{0.3}\text{MnO}_3$ is detected through XRD for the LSM 105 sample.

4. Conclusions

For LSM cathodes with different stoichiometries, half-cell long term thermal treatment shows that the polarization resistance is dominant for decreasing the half-cell performance. The A-site excessive LSM sample (LSM 105) experiences stronger bonding with the YSZ electrolyte. Cr species poison the cathode and

compromise the cell performance by first depositing and then being incorporated into the cathode perovskite structure through replacing Sr. Based on the above observations, the replacement of Sr by Cr in the LSM lattice structure is proposed to be responsible for the LSM cathode degradation. The electrochemical behavior of the cathodes is a combined result of microstructure evolution and elemental diffusion. Overall, the A-site deficient LSM stoichiometry (LSM 95) is preferred for cell performance improvement as it shows the smallest overall resistance when used as a cathode.

Acknowledgments

The authors acknowledge the financial support from Office of Naval Research under grant number N00014-11-1-0266.

References

- [1] S.C. Singhal, Solid State Ionics 152 (2002) 405–410.
- [2] N.Q. Minh, Solid State Ionics 174 (2004) 271–277.
- [3] S. Singhal, Am. Ceram. Soc. Bull. 82 (2003) 9601–9610.
- [4] W. Winkler, H. Lorenz, J. Power Sources 105 (2002) 222–227.
- [5] A. Weber, E. Ivers-Tiffey, J. Power Sources 127 (2004) 273–283.
- [6] E.O. Oh, H. Kim, D.C. Baek, J. Park, H.R. Kim, J.H. Lee, H.W. Lee, C.M. Whang, J.W. Son, Solid Oxide Fuel Cells 10 (SOFC-X) 7 (2007) 743–748.
- [7] M.A. Haider, S. McIntosh, J. Electrochem. Soc. 156 (2009) B1369–B1375.
- [8] J.A. Schuler, A.J. Schuler, Z. Wuillemin, A. Hessler-Wyser, C. Ludwig, J. Van Herle, Solid Oxide Fuel Cells 12 (SOFC XII) 35 (2011) 2001–2008.
- [9] K. Fujita, K. Ogasawara, Y. Matsuzaki, T. Sakurai, J. Power Sources 131 (2004) 261–269.
- [10] S. Taniguchi, M. Kadowaki, H. Kawamura, T. Yasuo, Y. Akiyama, Y. Miyake, T. Saitoh, J. Power Sources 55 (1995) 73–79.
- [11] S.P.S. Badwal, R. Deller, K. Fogar, Y. Ramprakash, J.P. Zhang, Solid State Ionics 99 (1997) 297–310.
- [12] E. Konyshova, H. Penkalla, E. Wessel, J. Mertens, U. Seeling, L. Singheiser, K. Hilpert, J. Electrochem. Soc. 153 (2006) A765–A773.
- [13] S.P. Jiang, Y.D. Zhen, Solid State Ionics 179 (2008) 1459–1464.
- [14] S.P. Jiang, S. Zhang, Y.D. Zhen, J. Mater. Res. 20 (2005) 747–758.
- [15] A. Nakajo, P. Tanasini, S. Diethelm, J. Van Herle, D. Favrat, J. Electrochem. Soc. 158 (2011) B1102–B1118.
- [16] L.G.J. de Haart, J. Mougin, O. Posdziech, J. Kiviah, N.H. Menzler, Fuel Cells 9 (2009) 794–804.
- [17] J.A. Schuler, Z. Wuillemin, A. Hessler-Wyser, C. Comminges, N.Y. Steiner, J. Van Herle, J. Power Sources 211 (2012) 177–183.
- [18] R. Lacey, A. Pramanick, J.C. Lee, J.I. Jung, B. Jiang, D.D. Edwards, R. Naum, S.T. Misture, Solid State Ionics 181 (2010) 1294–1302.
- [19] C.J. Fu, K.N. Sun, X.B. Chen, N.Q. Zhang, D.R. Zhou, Electrochim. Acta 54 (2009) 7305–7312.
- [20] T.G. Jin, K. Lu, Int. J. Hydrogen Energy 36 (2011) 4440–4448.
- [21] T.G. Jin, K. Lu, J. Power Sources 202 (2012) 143–148.
- [22] T.G. Jin, K. Lu, J. Power Sources 196 (2011) 8331–8339.
- [23] S.G. Li, W.Q. Jin, N.P. Xu, J. Shi, Solid State Ionics 124 (1999) 161–170.
- [24] W.L. Li, K. Lu, Z.B. Xia, J. Power Sources 237 (2013) 119–127.
- [25] T.G. Jin, K. Lu, J. Power Sources 197 (2012) 20–27.
- [26] Y.J. Leng, S.H. Chan, S.P. Jiang, K.A. Khor, Solid State Ionics 170 (2004) 9–15.
- [27] L.W. Tai, M.M. Nasrallah, H.U. Anderson, D.M. Sparlin, S.R. Sehlin, Solid State Ionics 76 (1995) 273–283.
- [28] S.P. Jiang, S. Zhang, Y.D. Zhen, J. Electrochem. Soc. 153 (2006) A127–A134.
- [29] Z.Y. Jiang, L. Zhang, K. Feng, C.R. Xia, J. Power Sources 185 (2008) 40–48.
- [30] S.P. Simmer, M.D. Anderson, G.G. Xia, Z. Yang, L.R. Pederson, J.W. Stevenson, J. Electrochem. Soc. 152 (2005) A740–A745.
- [31] K. Hilpert, D. Das, M. Miller, D.H. Peck, R. Weiss, J. Electrochem. Soc. 143 (1996) 3642–3647.
- [32] S.C. Paulson, V.I. Birss, J. Electrochem. Soc. 151 (2004) A1961–A1968.